Non-unit protection method for MMC-HVDC grids based on selective drop rate of voltage traveling waves

Dehghan Marvasti, Farzad; Mirzaei, Ahmad; Savaghebi, Mehdi; Lekić, Aleksandra; Popov, Marjan

DOI
10.1016/j.egyr.2024.03.045

Publication date
2024

Document Version
Final published version

Published in
Energy Reports

Energy Reports 11 (2024) 3740–3755

Contents lists available at ScienceDirect

Energy Reports

journal homepage: www.elsevier.com/locate/egyr

Research paper

Non-unit protection method for MMC-HVDC grids based on selective drop rate of voltage traveling waves

Farzad Dehghan Marvasti [a,b,*], Ahmad Mirzaei [b], Mehdi Savaghebi [c], Aleksandra Lekić [a], Marjan Popov [a]

[a] Delft University of Technology, Faculty of EEMCS, Mekelweg 4, Delft 2628CD, the Netherlands
[b] Department of Electrical Engineering, Yazd University, Yazd, Iran
[c] Department of Engineering Technology, Technical University of Denmark (DTU), Ballerup DK-2750, Denmark

ARTICLE INFO

Keywords:
Fault-generated voltage traveling wave
MMC-HVDC protection
Primary protection
Traveling wave protection

ABSTRACT

Fast, sensitive, and selective protection principles are one of the major challenges in the feasibility of modular multi-terminal (MMC) high voltage direct current (HVDC) grids. Rate of change of voltage (ROCOV) and transient-based solutions are the traditional and widely accepted protection principles. Despite the speed and practicality of these solutions, they generally suffer from sensitivity and selectivity issues, particularly when dealing with high-resistance faults and low-size current limiting inductors (CLIs). To improve upon these methods, this paper proposes a new primary protection method that utilizes a selective drop rate of fault-generated voltage traveling waves (TW) to detect internal DC line faults. This is achieved by a comprehensive analysis of the line-mode fault-generated voltage (LFGV) under various internal and external fault scenarios. As the key fault characteristics, the proposed method exploits the minimum points of initial LFGV and the corresponding time to form the basis of the proposed protection method. The effectiveness of this approach is evaluated using a four-terminal MMC-HVDC grid in PSCAD/EMTDC. Compared to ROCOV and transient-based solutions, the proposed method identifies internal faults up to 1250 Ω with fast response, while maintaining its practicality and independence to CLI size.

1. Introduction

Over the past decades, the application of MMC-HVDC transmission lines has been steadily rising due to the fast development of power electronics and the increasing demand for electrical energy (Sun et al., 2023). This technology can be exploited as a cost-effective solution for power transmission over long distances, e.g., from offshore wind power parks to the coast, and the interconnection of two grids with different frequencies.

Aside from these advantages, the limited fault-ride-through capability of MMC-HVDC systems and the vulnerability of their converters to devastating discharging fault currents are known as their main limitations. In such systems, it is essential to isolate only the faulty line/section of the system so that the remaining healthy sections can maintain their operation. Therefore, providing a fast, sensitive, and selective protection principle to ensure reliable system operation is extremely crucial (Sun et al., 2023; Chandio et al., 2023).

Generally, HVDC protective schemes can be divided into two major categories; primary and backup methods. Primary solutions use locally provided measurements for protective purposes, while double-ended measurements via a communication link are deployed in backup methods. Rate of change of voltage (ROCOV) and rate of change of current (ROCOC) based methods, with simple structure and fast response, are the most widely used primary protection schemes (Sneath et al., 2016; Leterme and Beerten, 2016). However, these methods have reliability issues in detecting high resistance faults, which limit their application. Other primary methods have been presented using voltage change rate of current limiting inductors (CLIs) (Li et al., 2017; Li et al., 2018; Liu et al., 2017). Although these methods show better overall performance in comparison to ROCOV and ROCOC, their performance depends highly on the CLI level, i.e., inaccurate performance has been reported in HVDC systems with small CLI (Jovcic et al., 2018; Saizhao et al., 2021).

Traveling wave (TW)-based methods are promising primary protective solutions with fast and accurate responses (Zhang et al., 2021; Li et al., 2020a; Yu et al., 2021Lan et al., 2021; Zhang et al., 2022). The

* Corresponding author at: Delft University of Technology, Faculty of EEMCS, Mekelweg 4, Delft 2628CD, the Netherlands.
E-mail address: F.DehghanMarvasti@tudelft.nl (F. Dehghan Marvasti).

https://doi.org/10.1016/j.egyr.2024.03.045
Received 12 September 2023; Received in revised form 6 February 2024; Accepted 19 March 2024
Available online 23 March 2024

approach presented in Zhang et al. (2021) relies solely on timing characteristics of the voltage TWs to distinguish internal faults and requires high sampling frequency, facing difficulties when dealing with high-resistance external faults. The works presented in Li et al. (2020a) and Yu et al. (2021) adopt new directional criteria based on TWs for internal fault detection. These methods are categorized as pilot protections since they rely on measurements from both sides of the line. Nevertheless, they suffer from slower fault detection speed and potential reliability issues of the communication link compared to primary solutions. Alternative TW-based methods like those proposed in Lan et al. (2021) and Zhang et al. (2022), aim to provide more robust solutions for dealing with high-resistance faults. However, they lack supporting the entire length of the transmission line (Lan et al., 2021) and complex structure, requiring extensive data samples for calculations (Zhang et al., 2022). In (Zhang et al. 2019; Li et al., 2019) and Xiang et al. (2019), Wavelet-transform (WT) based protection principles by comparing the frequency response differences of TWs during internal and external faults have been presented. Apart from promising performance, the analytical approach and the maximum fault detection capability in these methods are relatively low. By focusing on the frequency-domain characteristics of TWs, an ultra-high-speed protection scheme has also been proposed in Saleh et al. (2020), which requires a very high sampling frequency. Employing an estimation of fault resistance, a new protective method is introduced in Yu et al. (2023a), despite the slower protection speed due to fault location dependency. In Lan et al. (2022), a WT-based protection method with a low computational burden has been adopted. However, this method can be vulnerable to environmental noise.

To enhance the sensitivity and selectivity of primary protection methods, pilot protection principles are implemented as the backup schemes, e.g., current differential protection (Li et al., 2009; Wang et al., 2021). However, the high dependency of the current differential method's performance on distributed capacitance of the transmission line is known as its main shortcoming. This conventional method has been enhanced by defining other variants of the current differential protection (Chu, 2019; Li et al., 2020b). Utilizing this new criterion, the effect of distributed capacitance on the method's performance is mitigated and the fault detection response is enhanced (Zhang et al., 2023). However, these methods are generally complicated, and the computational burden makes them technically hard to implement in practice. Other researchers have focused on adopting protective methods based on under-fault transient energy ratio and specific frequency current of DC filters (Dai et al., 2020; Zaang et al., 2019) as well as the behavior of characteristic harmonic impedances (Marvasti et al., 2020). The realization of these methodologies is still limited in practice, especially for MMC-HVDC grids due to their high dependency on DC line filters. The works of (Wang et al., 2019; Farshad, 2021; Yu et al., 2023b) adopt protection methods based on similarity measures of voltage TWs as pilot protective principles with high sensitivity and selectivity. However, tightly synchronized data is necessary for reliable operation of Wang et al. (2019) and Farshad (2021).

According to the literature, ROCOV-based methods, while effective up to a certain fault resistance (e.g., 100 ohms), exhibit reduced reliability beyond that point, making it challenging to distinguish between external low-resistance and internal high-resistance faults. Furthermore, other transient-based methods heavily rely on the CLI size for reliable operation and can lose sensitivity and selectivity under high-resistance faults. To address these limitations, this study enhances the well-known ROCOV and transient-based protection principles in terms of sensitivity and selectivity. To this end, an extensive analytical analysis of LFGV, by improving the presentation of modal propagation function and modal wave impedances, is conducted to identify the areas for improvement. An in-depth analytical study reveals the key factors responsible for the distinct behavior observed under internal and external faults. Leveraging these insights, a significant enhancement to the traditional ROCOV and transient-based methods is proposed, which relies on the selective voltage drop rate of LFGV within a specific time window. Accurate consideration of the data window for extracting the minimum point of the LFGV and applying a new criterion based on the selective drop rate of voltage are the main features of the proposed protection method. The proposed method, primarily developed to operate within the initial fault-generated TW, offers the following key contributions:

- Improved sensitivity and selectivity compared to the traditional ROCOV and transient-based solutions, surpassing even some of the recent TW-based methods.
- Thorough and improved analytical investigation of LFGV to support the proposed method.
- Using analytical calculations to significantly facilitate the process of protective threshold determination and improve the adaptability of the proposed solution.

These features and the performance of the proposed protection method are validated using a four-terminal MMC-HVDC grid, simulated in PSCAD/EMTDC.

The remainder of the paper is organized as follows. The basic theory of fault TWs and the analytical extraction of LFGV are presented in Section 2. The proposed protection method is elaborated in Section 3. The performance of the proposed method is assessed under various fault scenarios in Section 4. Further analysis regarding the robustness of the presented method is then provided in Section 5, and finally, the concluding remarks are presented in Section 6.

2. Fault-generated voltage traveling wave

A four-terminal ±500 kV MMC-HVDC transmission line, employing half-bridge (HB) converters, is considered the investigated system. This grid is chosen to investigate the behavior of LFGV under different fault scenarios. The outcomes of these investigations serve as the basis for establishing the proposed protection method. The schematic diagram of the test system and its parameters are presented in Fig. 1 and Table 1, respectively.

The HVDC system simulated in PSCAD/EMTDC utilizes four 300 km overhead transmission lines, modeled by the frequency-dependent line parameters. The CLIs are employed to lower the requirement on the DC protection (Chen et al., 2022). Measurement units and protective relays are installed at both ends of each line indicated by R_1–R_4 and $R_1^{'}$–$R_4^{'}$. The performance of the proposed method is assessed under different internal and external faults at various locations, indicated by f_1–f_5. The cases include single pole-to-ground (SPG), i.e., positive pole-to-ground (PTG) and negative pole-to-ground (NTG) faults, as well as pole-to-pole (PTP) faults.

2.1. Traveling wave theory

As broadly discussed in many studies, transmission lines can be modeled with a distributed equivalent circuit as follows (Liu et al., 2023):

$$\begin{cases} \dfrac{\delta u(x,t)}{\delta x} + Ri(x,t) + L\dfrac{\delta i(x,t)}{\delta t} = 0 \\ \dfrac{\delta i(x,t)}{\delta x} + Gu(x,t) + C\dfrac{\delta u(x,t)}{\delta t} = 0 \end{cases} \tag{1}$$

where R, L, G, and C are the resistance, inductance, conductance, and capacitance per unit length of the transmission line, respectively. Due to the coupling effect between the lines of a bipolar HVDC system, the electrical quantities of the system should be decoupled to improve the effectiveness of the fault analysis. The decoupling process can be performed using a decoupling matrix as expressed in (2):

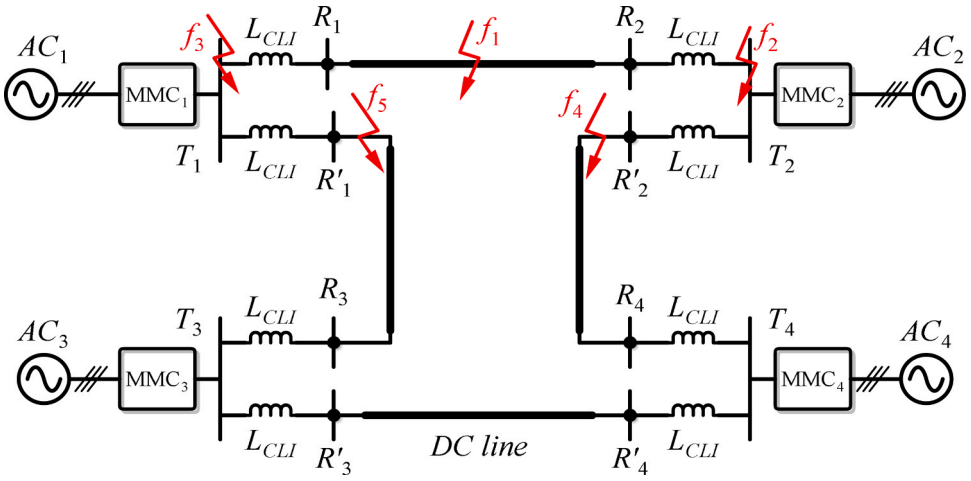

Fig. 1. Schematic diagram of the MMC-HVDC test grid.

Table 1
Parameters of the four-terminal MMC-HVDC grid.

System parameters	MMC_1, MMC_2, MMC_3, and MMC_4
Rated power (MW)	2000
Rated DC voltage, U_{dc} (kV)	±500
Rated AC voltage (kV)	400
CLI (mH)	200
Converter arm inductor (mH)	40
Number of submodules per arm	200
Submodule capacitance (μF)	8000

$$\begin{bmatrix} u_0 \\ u_1 \end{bmatrix} = \frac{1}{\sqrt{2}} \begin{bmatrix} 1 & 1 \\ 1 & -1 \end{bmatrix} \begin{bmatrix} u_p \\ u_n \end{bmatrix}, \begin{bmatrix} i_0 \\ i_1 \end{bmatrix} = \frac{1}{\sqrt{2}} \begin{bmatrix} 1 & 1 \\ 1 & -1 \end{bmatrix} \begin{bmatrix} i_p \\ i_n \end{bmatrix} \tag{2}$$

In this expression, positive and negative pole voltages (u_p and u_n) and currents (i_p and i_n) are resolved into their equivalent zero- (u_0 and i_0) and line-mode (u_1 and i_1) components (Liu et al., 2023). After decoupling the electrical quantities, the general solution for the zero- and line-mode DC voltages and currents can be expressed as follows:

$$\begin{cases} U_0(x) = U_{f0}e^{-\gamma x} + U_{b0}e^{\gamma x} \\ I_0(x) = I_{f0}e^{-\gamma x} - I_{b0}e^{\gamma x} \end{cases}, \frac{U_{f0}}{I_{f0}} = \frac{U_{b0}}{I_{b0}} = Z_{c0}$$
$$\begin{cases} U_1(x) = U_{f1}e^{-\gamma x} + U_{b1}e^{\gamma x} \\ I_1(x) = I_{f1}e^{-\gamma x} - I_{b1}e^{\gamma x} \end{cases}, \frac{U_{f1}}{I_{f1}} = \frac{U_{b1}}{I_{b1}} = Z_{c1} \tag{3}$$

where U and I represent voltage and current, respectively. Subscripts "0" and "1" refer to zero- and line-mode components, respectively. Subscripts "f" and "b" stand for forward and backward TWs, respectively. Z_{c0}, and Z_{c1} are also the zero- and line-mode wave impedances, respectively. Finally, γ is the propagation constant.

2.2. Fault-generated voltage at fault point

During PTG faults, the variation of the zero- and line-mode voltage at the fault position can be expressed as follows (Zhang et al., 2012):

$$\Delta u_{flt,0} = \frac{-\sqrt{2}U_{dc}.Z_0}{s(Z_0 + Z_1 + 2R_f)}, \Delta u_{flt,1} = \frac{-\sqrt{2}U_{dc}.Z_1}{s(Z_0 + Z_1 + 2R_f)} \tag{4}$$

where U_{dc} is the rated DC voltage of the line and R_f is the fault resistance. Furthermore, Z_0 and Z_1 are the Thévenin-equivalent zero- and line-mode impedances observed from the fault location, respectively. Similarly, the zero- and line-mode voltage variations under NTG faults can be given as:

$$\Delta u_{flt,0} = \frac{\sqrt{2}U_{dc}.Z_0}{s(Z_0 + Z_1 + 2R_f)}, \Delta u_{flt,1} = \frac{-\sqrt{2}U_{dc}.Z_1}{s(Z_0 + Z_1 + 2R_f)} \tag{5}$$

For PTP faults, the zero- and line-mode voltage waveforms can be expressed as follows:

$$\Delta u_{flt,0} = 0\ ,\ \Delta u_{flt,1} = \frac{-2\sqrt{2}U_{dc}.Z_1}{s(2Z_1 + R_f)} \tag{6}$$

According to the equations, the line-mode component has lower attenuation constant, higher wave velocity and exists under all fault types. Therefore, LFGV is adopted for the design of the proposed non-unit protection method based on fault-generated voltage TW. In this perspective, first, the frequency-domain expression of LFGV at the fault point and then at the terminal R_1 under internal and external faults is precisely formulated. Afterwards, the time domain response of LFGV is extracted using the inverse Laplace transform to fully investigate the fault characteristics. Finally, a new protection method is proposed based on the time-domain analysis. This criterion is detailed for various fault scenarios in the next subsections.

2.3. LFGV at R_1 in case of internal faults

To derive the frequency-domain expression of the LFGV at terminal R_1 under an internal fault (f_1 in Fig. 1), the equivalent line-mode circuit of the system at the fault point should be closely analyzed (Fig. 2).

When internal fault occurs, the generated LFGV from the fault point propagates along the transmission line. As shown in Fig. 2, the relationship of LFGV at the fault point ($\Delta u_{flt,1}$) based on the fault type can be expressed by Eqs. (4)–(6) wherein Z_0 and Z_1 are determined as follows:

$$\begin{cases} Z_0 = Z_{l0} || Z_{r0} = Z_{c0}/2 \\ Z_1 = Z_{l1} || Z_{r1} = Z_{c1}/2 \end{cases} \tag{7}$$

where Z_{l0} and Z_{r0} are the zero-mode, and Z_{l1} and Z_{r1} are the line-mode wave impedances seen from the fault point to each side of the line. Assuming the forward direction from the fault point and DC terminals to the transmission line, these impedances can be derived from Eq. (3) as follows:

$$\begin{cases} Z_{l0} = U_{fl0}/I_{fl0} = Z_{c0} \\ Z_{r0} = U_{fr0}/I_{fr0} = Z_{c0} \end{cases}, \begin{cases} Z_{l1} = U_{fl1}/I_{fl1} = Z_{c1} \\ Z_{r1} = U_{fr1}/I_{fr1} = Z_{c1} \end{cases} \tag{8}$$

where U_{fl0} and U_{fr0} are the fault-generated zero-mode forward voltages propagating to each section of the line. Also, U_{fl1} and U_{fr1} are the corresponding line-mode counterparts. Similarly, the fault-generated zero-mode forward currents are shown by I_{fl0} and I_{fr0}, whilst I_{fl1} and I_{fr1} are

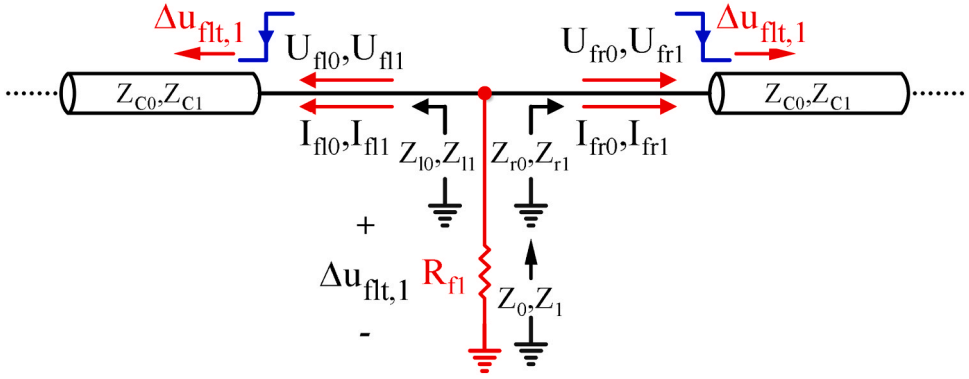

Fig. 2. LFGV generation and propagation at fault point in case of internal faults.

the corresponding line-mode counterparts.

After being generated at the fault point, LFGV propagates along the line and is consequently affected by the propagation function before reaching the line inductive end (R_1). At this point, the traveling wave is partially reflected to the transmission line and refracted to the converter side. Therefore, LFGV at R_1 (Δu_{R1}) which is the summation of the backward (Δu_{b1}) and the reflected forward (Δu_{f1}) TWs, can be obtained based on the terminal equivalent circuit, illustrated in Fig. 3:

$$\Delta u_{R1} = \Delta u_{b1} + \Delta u_{f1} = \Delta u_{flt,1} e^{-\gamma_1(s)x} + \Gamma_1 \Delta u_{flt,1} e^{-\gamma_1(s)x} = \left(1+\Gamma_1\right)\Delta u_{flt,1} e^{-\gamma_1(s)x} \tag{9}$$

$$\Gamma_1 = \frac{Z_{con}||(sL_{CLI}+Z_{c1}) + sL_{CLI} - Z_{c1}}{Z_{con}||(sL_{CLI}+Z_{c1}) + sL_{CLI} + Z_{c1}} \tag{10}$$

$$Z_{con} = R_c + sL_c + \frac{1}{sC_c} \tag{11}$$

In these equations, Γ_1, γ_1, and x are the line-mode reflection coefficient, line-mode propagation function, and fault location, respectively. Also, Z_{con} stands for the converter's equivalent impedance, i.e., equivalent to a series RLC circuit (Chen et al., 2022); hence, R_c=2 (R_{arm}+R_{on})/3, L_c=2L_{arm}/3, and C_c=6C_{sm}/N where R_{arm}, L_{arm}, and C_{sm} are the arm resistance, arm inductance, and capacitance of the sub-module, respectively. Moreover, R_{on} and N are the on-state resistance of the entire inserted sub-modules in each arm and the number of inserted sub-modules, respectively.

Line-mode propagation coefficient, $\gamma_1(s)$, and modal wave impedances, Z_{c0} and Z_{c1}, as expressed by Eqs. (12) and (13), are frequency-dependent in nature, where r_i, L_i, g_i and C_i, $i \in 0,1$ are the zero/line-mode resistance, inductance, conductance, and capacitance per unit length of the transmission line.

$$\gamma_i(s) = \sqrt{(r_i(s) + jwL_i(s)).(g_i + jwC_i(s))} \tag{12}$$

$$Z_{ci}(s) = \sqrt{(r_i(s) + jwL_i(s))/(g_i + jwC_i(s))} \tag{13}$$

The frequency dependency is evident in Fig. 4(a) and (b), where the magnitude of the modal propagation functions ($e^{-\gamma_i(s)x}$) and modal wave impedances ($Z_{ci}(s)$) is depicted, respectively. Therefore, vector fitting (VF) with a non-linear rational approximation is used to effectively incorporate $e^{-\gamma_i(s)x}$ and $Z_{ci}(s)$ into Eqs. (9) and (10):

$$e^{-\gamma_1(s)x} \cong F(s) = \sum_{k=1}^{n} \frac{C_k}{s - A_k} + D \tag{14}$$

$$Z_{c0}(s) \cong F_{c0}(s) = \sum_{k=1}^{n} \frac{C_k}{s - A_k} + D \tag{15}$$

where C_k and A_k are complex residues and poles. respectively. Also, D is a real constant. Based on Fig. 4(b), the deterioration of line-mode components is significantly lower than

zero-mode counterparts, hence, only $Z_{c0}(s)$ is modelled by VF in Eq. (13), which also alleviates the computational burden of the calculations. Finally, the frequency-domain expression of LFGV at R_1 can be deducted from Eqs. (4)–(15) as follows:

$$\Delta u_{R1} = \left(1+\Gamma_1\right)\Delta u_{flt,1} F(s) \tag{16}$$

The time-domain expression of LFGV can be deducted by applying the inverse Laplace transform to Eq. (16) and substituting the variables

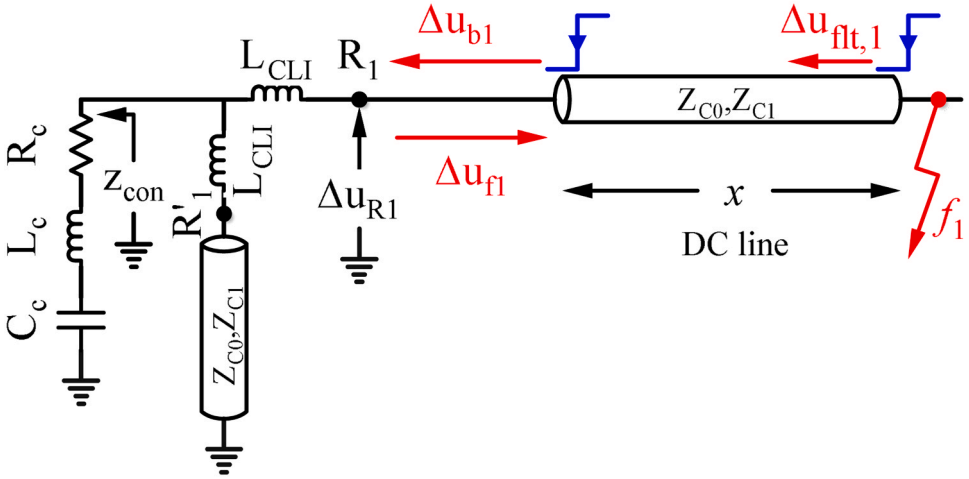

Fig. 3. Equivalent circuit at R_1 in case of internal faults.

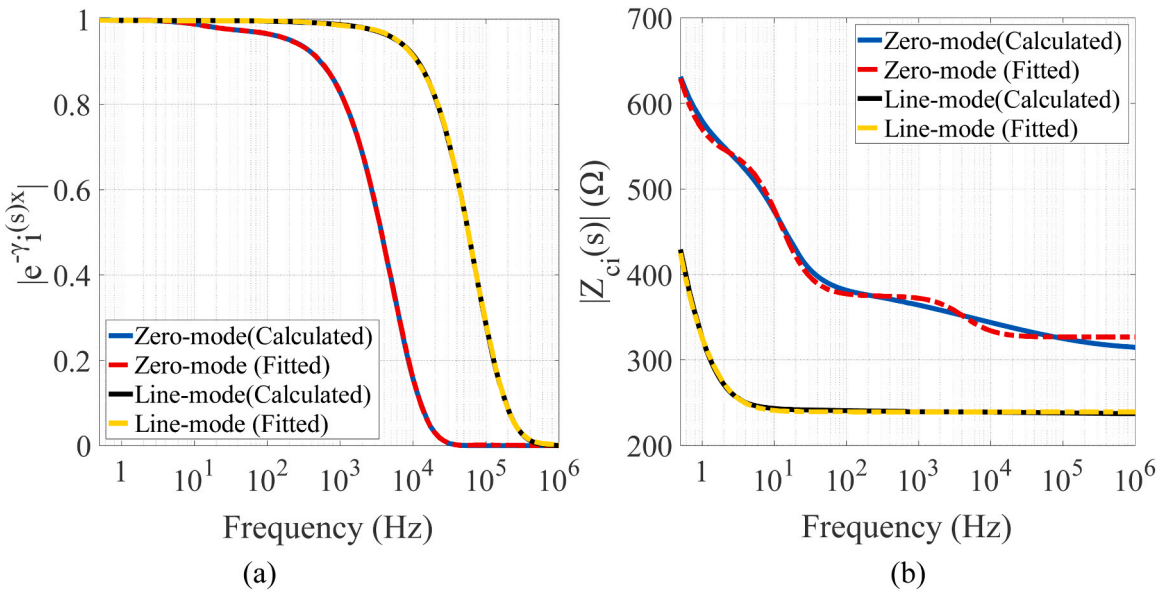

Fig. 4. Frequency characteristic: a) modal propagation functions and b) modal wave impedances.

with the relevant parameters. However, as Eqs. (14) and (15) use multiple terms to enhance the accuracy of the LFGV, the derived time-domain expression consists of many exponential terms. Considering the challenge of presenting these results in their algebraic form and the complexity of the analysis, graphical representation of the results is chosen for the time-domain analysis in this paper. Note that in the entire analytical calculations of this paper numerous fault scenarios, including all types of internal and external faults (SPG and PTP faults) for various fault resistance and location sets, are considered. This ensures the generality of the consequent conclusions.

Several example cases are chosen and depicted in Fig. 5 to summarize the time-domain analysis during internal faults. Fig. 5(a) and (b)

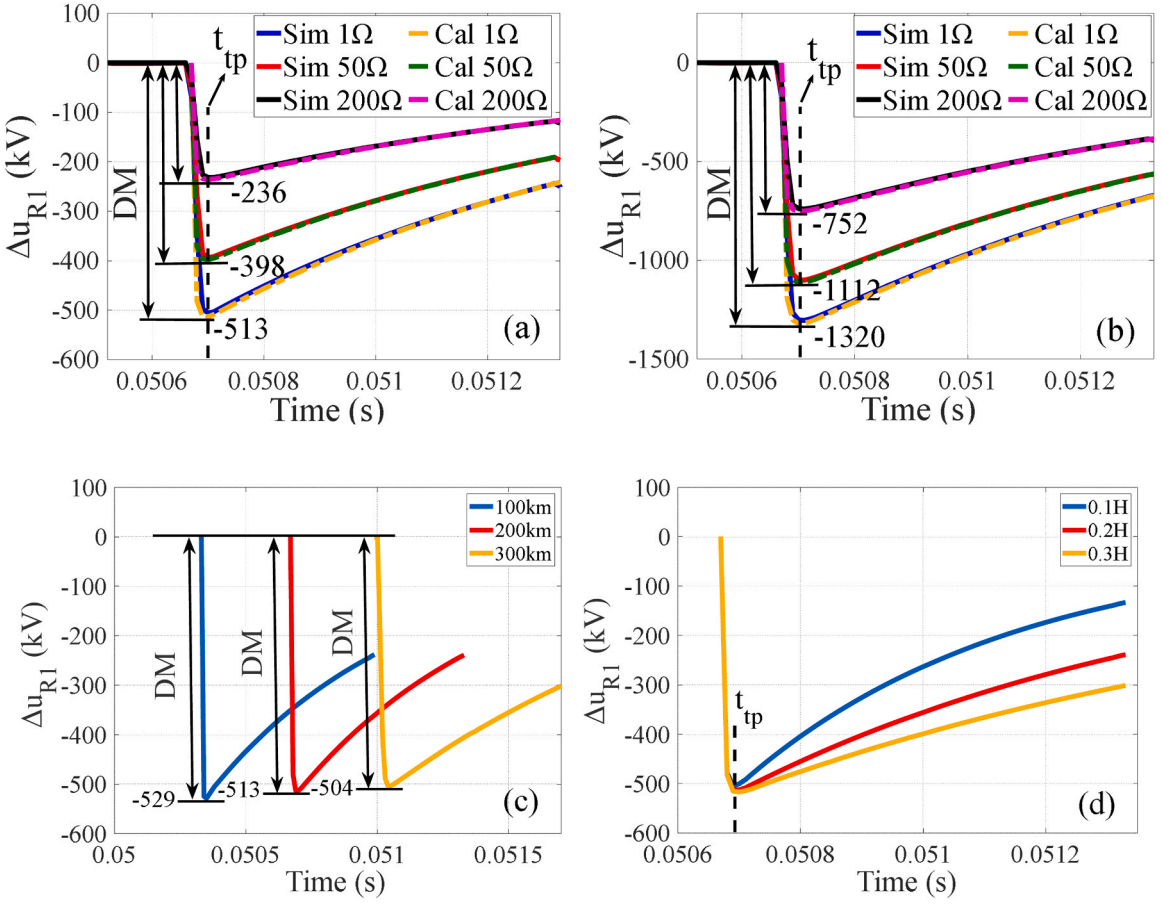

Fig. 5. Impact of various parameters on LFGV: a) fault resistance under PTG faults, b) fault resistance under PTP faults, c) propagation function, d) CLI.

illustrate the time-domain response of LFGV under PTG and PTP faults at 200 km distance for various R_f sets, respectively. A comparison between the analytical calculations (Cal) with the simulation results (Sim) is also provided in these figures to demonstrate the precision of the analytical calculations. It is readily seen that as the fault resistance increases, the drop magnitude (DM) of the LFGV, measured from zero to the minimum point of the waves (wave-heads), diminishes for both fault types. Moreover, while the position of the wave-heads in time (t_{tp}) changes slightly under various fault resistances, they are observed almost immediately after fault initiation for all scenarios. Although the only factor affecting t_{tp} is the propagation function, this impact is negligible as LFGV is used. According to Fig. 5(a) and (b), the voltage drop rates under PTP faults are markedly greater than those under similar PTG faults.

On the other hand, as shown in Fig. 5(c), the impact of the fault location on the DMs under PTG faults, originating from the propagation function, i.e., $F(s)$ in Eq. (16), is not significant and can be neglected. Finally, Fig. 5(d) highlights that the effect of CLI level on the DMs is hardly noticeable. Nevertheless, the rising rate of the waveforms after passing t_{tp} is sharper for smaller CLI sizes.

According to the presented analyzes, it can be concluded that fault resistance is the most influential factor affecting the LFGV under internal faults.

2.4. LFGV at R_1 in case of forward external faults

Similar to the conducted analysis for internal faults, the equivalent line-mode circuit of the system under forward external faults (f_2 in Fig. 1) is depicted in Fig. 6.

LFGV at the fault point ($\Delta u_{flt,1}$) is given with Eqs. (4)–(6), in where Z_0 and Z_1 can be obtained as follows (Fig. 6):

$$\begin{cases} Z_0 = Z_{l0}||Z_{r0} = \dfrac{U_{fl0}}{I_{fl0}}||\dfrac{U_{fr0}}{I_{fr0}} = \left(sL_{CLI} + Z_{c0}\right)||(Z_{con}||\left(sL_{CLI} + Z_{c0}\right)\right) \\ Z_l = Z_{l1}||Z_{r1} = \dfrac{U_{fl1}}{I_{fl1}}||\dfrac{U_{fr1}}{I_{fr1}} = \left(sL_{CLI} + Z_{c1}\right)||(Z_{con}||\left(sL_{CLI} + Z_{c1}\right)\right) \end{cases} \quad (17)$$

The effect of CLI on Λ_1, i.e., LFGV at R_2, can be expressed as follows:

$$\begin{cases} \Delta u_{r1} = \Delta u_{flt,1}\Lambda_1 \\ \Lambda_1 = \dfrac{Z_{c1}}{Z_{c1} + sL_{CLI}} \end{cases} \quad (18)$$

After propagating through the transmission line and being affected by the line propagation function, LFGV reaches the line boundary as shown in Fig. 7. At this point, the frequency-domain expression of LFGV which is the summation of distorted backward traveling wave and its reflected waveform can be obtained as follows:

$$\Delta u_{R1} = \Delta u_{b1} + \Delta u_{f1} = \left(1 + \Gamma_1\right)\Delta u_{flt,1}\Lambda_1 F(s) \quad (19)$$

where Γ_1 and $F(s)$ is derived from Eqs. (10) and (14) for x=l, respectively. The time-domain response of the LFGV can be then computed using the inverse Laplace transform on Eq. (19).

The results are presented in Fig. 8 where several comparisons between the analytical calculations and simulation results are presented. As shown in Fig. 8(a) and (b), a higher R_f not only lowers the DMs of the LFGV, but also reduces the required time to reach the wave-heads ($t_{tp200} < t_{tp50} < t_{tp1}$) for all fault types. Moreover, the wave heads have smoother shapes compared to those under internal faults. This behavior is mainly due to the impact of CLI on the LFGVs. In similar conditions, the DMs under internal faults are more significant than those under forward external faults.

On the other hand, according to Fig. 8(c), higher values of CLI slightly decrease the DMs but greatly increase the time of the wave-heads ($t_{tp0.3} > t_{tp0.2} > t_{tp0.1}$). Compared to the internal fault cases with similar fault resistances, much smoother wave shapes and lower DMs are expected under forward external faults.

2.5. LFGV at R_1 in case of reverse external faults

The expression of LFGV under reverse external faults can be derived from Fig. 9, as presented by Eq. (20). This case is identical to that of the forward external faults observed at R_2:

$$\Delta u_{R1} = \Delta u_{flt,1}\Lambda_1 \quad (20)$$

where Λ_1 reflects the impact of CLI on the LFGV as presented by Eq. (18). Also, $\Delta u_{flt,1}$ is expressed by Eqs. (4)–(6), in which Z_0 and Z_1 are calculated according to Eq. (17).

The graphical evaluations of the results coupled with the comparison of the analytical calculations with the simulation results are presented in Fig. 8(d)–(f). The conclusions here are similar to those under the forward external faults presented in subsection 2.4.

3. Proposed protection method

In this section, the main factors considered in the design of the proposed fault identification criterion are first discussed. Afterward, the formulation of the criterion and proposed protection algorithm are presented.

3.1. Design consideration of fault identification criterion

As shown earlier, it can be summarized that fault resistance and CLI are the most influential factors, in determining the smoothness of the waveforms, the time position of the wave-heads, and the level of DMs.

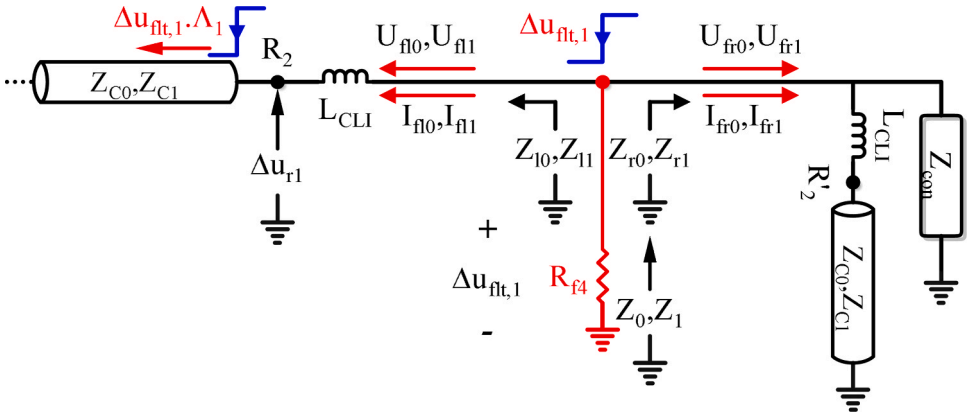

Fig. 6. Equivalent circuit at R_2 in case of forward external faults.

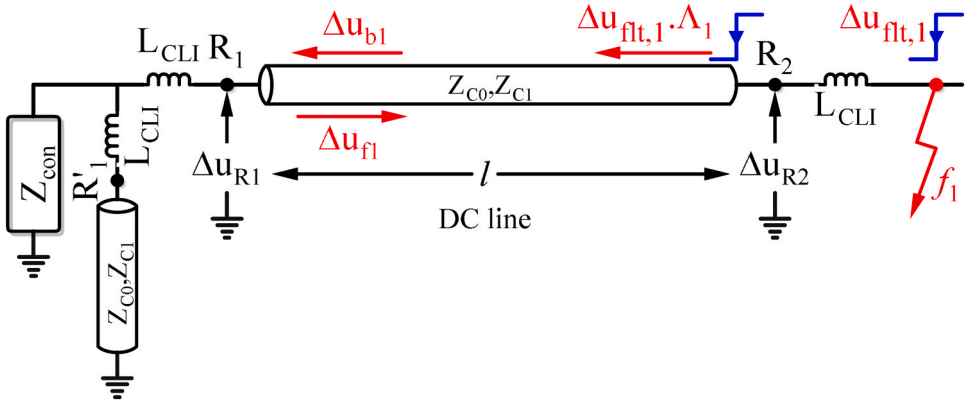

Fig. 7. Equivalent circuit at R_1 during a forward external fault.

Hence, internal and external faults can be accurately distinguished through the voltage drop magnitude of LFGV and the required time to reach its wave head. These two features are exploited in the proposed fault identification method. In this regard, the slope of the straight lines that connect the starting points of the LFGVs to their wave heads is measured. These straight lines are shown with black dashed lines in Fig. 10 for various fault scenarios, i.e., *SI* for a 750 Ω fault at the line end as well as SE_1 and SE_2 for 1 Ω internal and reverse external faults, respectively. Application of these slopes is the key factor in the design of the proposed protection method as the impact of DM and time position of wave-heads (t_{tp}) are reflected in them at the same time.

According to the presented assessment of the most challenging fault scenarios in Fig. 10, a reliable process for threshold calculation of the protection relays is seen. In other words, when the protective relays are set properly in a way that a high-resistance internal fault, with R_f=750 Ω for instance, can be classified from severe external faults, distinguishing between other internal and external fault scenarios is ensured. This conclusion is derived from the analysis presented in Section 2, where the impact of fault resistance and CLI on internal and external faults are investigated. Hence, the generality of the setting calculation principle is guaranteed.

Furthermore, the wave-heads of the LFGVs during internal faults are observed faster than those during external faults as shown earlier. Therefore, a shorter time window, Δt_s, is considered for the calculation of the slopes to speed up the fault detection process. Determination of Δt_s is crucial in the design of the proposed protection method. As discussed in Section 2, the position of t_{tp} is almost constant under internal faults, while it changes under external faults depending on CLI size and fault resistance. The analysis in Section 2 revealed that t_{tp} is around 20–30 μs after fault inception under internal faults, while depending on the fault resistance and CLI size, it is observed at around 250–800 μs under external faults. Therefore, Δt_s=250 μs is set in this work.

During Δt_s, the slope of the *SI* line, which is related to the internal fault, is significantly sharper than those of the external faults, and ST_1 is sharper than ST_2. Therefore, ST_1 is assigned as the threshold line ($ST_{1\text{-}s}$) in a sense that lines with sharper slopes should trigger the protection principle as an indication of internal fault occurrence.

As discussed in Section 2, the level of DM under PTP faults is higher than SPG faults. Thus, PTP faults produce generally sharper straight lines than similar SPG internal faults. Therefore, there can be some external PTP fault scenarios that produce sharper straight lines compared to some internal SPG faults, and inevitably cause maloperation of the proposed protection criterion. To tackle this challenge, an effective solution is to firstly identify the faulty pole and then adjust the threshold line. The extraction of corresponding threshold lines for PTP faults can be carried out by repeating the process explained in Fig. 10, as illustrated in Fig. 11. Here, the lines ST_1 and ST_2 are the candidate threshold lines. However, due to the sharper slope, ST_1 is chosen as the threshold line under PTP faults ($ST_{1\text{-}p}$).

3.2. Formulation of the proposed fault identification criterion

The proposed protection criterion, which is hereafter referred to as the selective drop rate of voltage (SDR_v), is defined as follows:

$$SDR_v = \frac{\min\{\Delta u_{R1}(n_0-1, n_0, \ldots, n_0+n\Delta t)\} - m_u}{1000.(n_{\min}-(n_0-1))} \tag{21}$$

SDR_v uses a series of DC voltage samples at R_1 (Δu_{R1}) over a data window of Δt_1 which is shown by $\Delta u_{R1}(n_0\text{-}1, n_0, \ldots, n_0+n\Delta t)$ in Eq. (21). Therefore, the length of Δt_1 is $(n+2)\Delta t$, while Δt is the sampling time interval. In addition, $\min\{\Delta uR_1\}$ captures the voltage at the wave head of LFGV. m_u is also the median of the steady-state quantities of Δu_{R1}. Finally, n_0 and n_{min} refer to the sample number of the starting point and wave head of LFGV, respectively. The protective criterion trips when the setting threshold based on the fault type is exceeded. This setting threshold is defined as in Eq. (22):

$$\begin{cases} SDR_v < V_{th-s}, V_{th-s} = 1.25 \times S_{T_1-s} \rightarrow SPG\ internal\ fault \\ SDR_v < V_{th-p}, V_{th-p} = 1.25 \times S_{T_1-p} \rightarrow PTP\ internal\ fault \end{cases} \tag{22}$$

where $ST_{1\text{-}s}$ and $ST_{1\text{-}p}$ are the slopes of the threshold lines under SPG and PTP faults, respectively. Based on the description of Figs. 10 and 11, $ST_{1\text{-}s} = -33$, hence $V_{th\text{-}s} = -41$, and $ST_{1\text{-}p} = -56$, hence $V_{th\text{-}p} = -70$ are considered as the thresholds in Eq. (22).

It is evident that the definition of the proposed protection method is similar to ROCOV-based solutions. However, there are differences that make the proposed method more robust and reliable. The first advantage is the careful determination of Δt_1, by which the wave head can be precisely identified. Through this selection, the proposed method produces higher outputs under internal faults, which improves its performance in distinguishing internal and external faults. This enhanced performance is also observed under noisy conditions wherein ROCOV-based solutions suffer from inaccurate calculation of dv/dt. Moreover, the impact of fault resistance and CLI size on the LFGV is fully investigated. This is another advantage of the proposed protection method in comparison to ROCOV and other transient-based solutions, where the calculation of DC line voltage (in contrast to LFGV) at both sides of the CLI is performed without careful analytical considerations. Moreover, a more accurate and comprehensive analytical representation of the LFGV under various fault scenarios is presented in this study. The extensive modelling of modal propagation functions, $e^{-\gamma_i(s)x}$, and modal wave impedances, $Z_{ci}(s)$, contributes to a more accurate representation of various fault cases, which also leads to an improved determination of Δt_s, extraction of the minimum wave points and calculation of SDR_v.

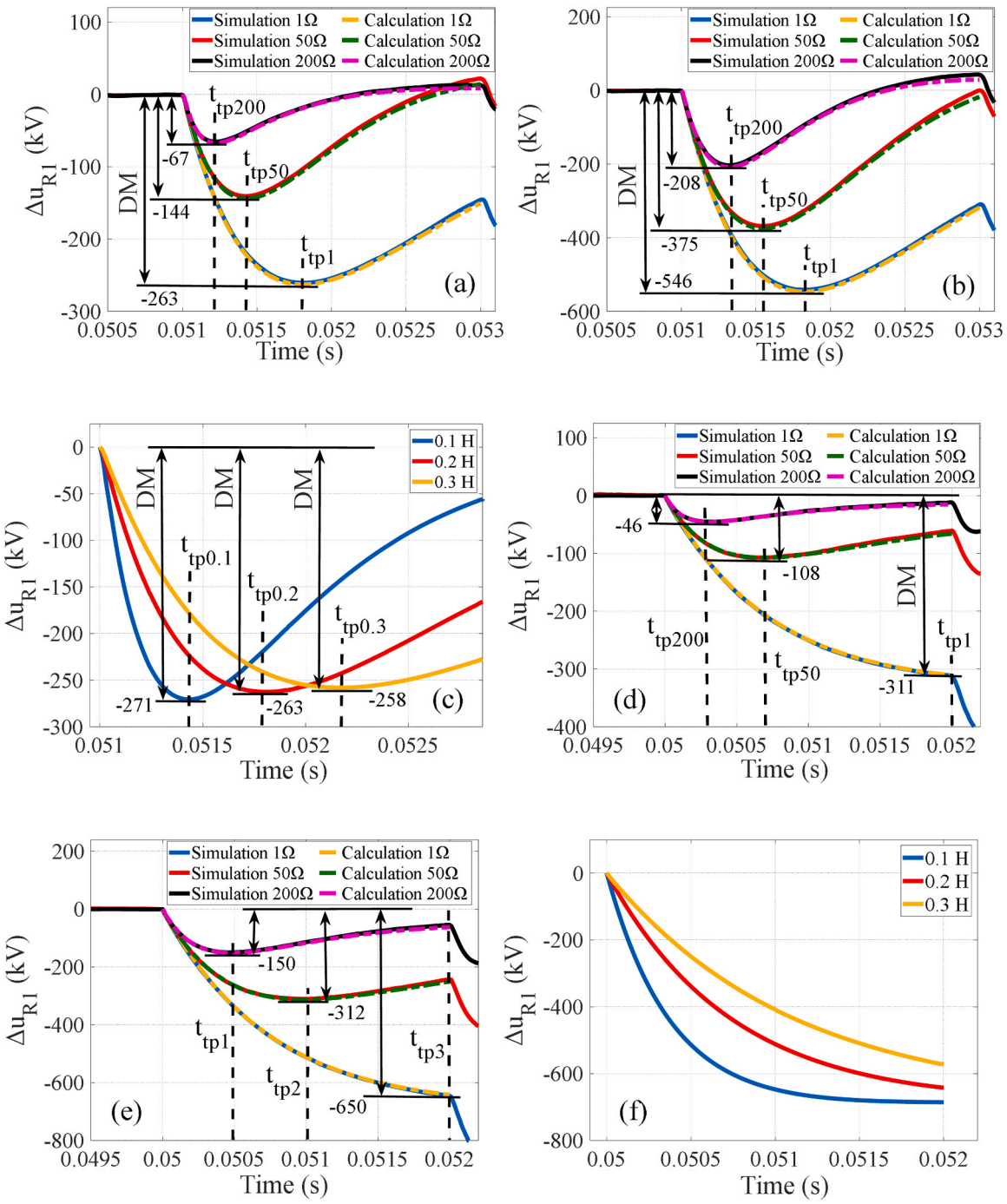

Fig. 8. Impact of various parameters on LFGV: a) fault resistance under PTG forward external faults, b) fault resistance under PTP forward external faults, c) CLI under PTG forward external faults, d) fault resistance under PTG reverse external faults, e) fault resistance under PTP reverse external faults, f) CLI under PTG reverse external faults.

3.3. Protection algorithm

The schematic diagram of the overall protection algorithm is depicted in Fig. 12. A start-up unit (SU) in the form of an undervoltage criterion is considered as the fault detection criterion to distinguish between faults and normal operation. The definition is expressed as follows:

$$\{\Delta u_{R1} < -V_{ths} \tag{23}$$

where Δu_{R1} is the pole voltage gradient at R_1. Also, V_{ths} is the threshold which should be lower than the voltage variation under normal operation. Therefore, it is considered 25 kV ($0.05V_r$) in this work. The first voltage sample at which Eq. (23) is satisfied is denoted by n_0. This sample is used for defining SDR_v.

As explained in the previous subsection, the faulty pole should be identified prior to fault identification to adjust the setting threshold. It can be seen in Eqs. (4)–(6) that under PTG, NPG, and PTP faults, the zero-mode voltage component is negative, positive, and zero, respectively. This implies that the zero-mode voltage component can be used as a fault pole identification criterion (FPIC). Therefore, accumulation of the zero-mode voltage at R_1 over the 5-sample data window of Δt_s is considered for FPIC as follows:

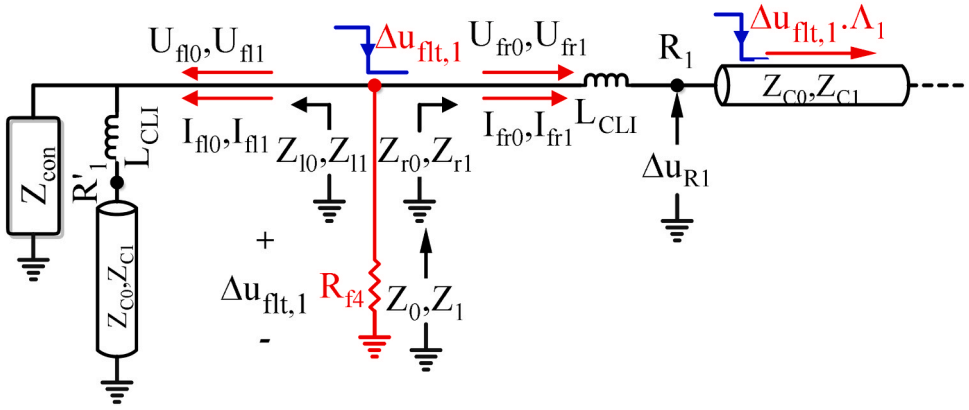

Fig. 9. Equivalent circuit at R_1 in case of reverse external faults.

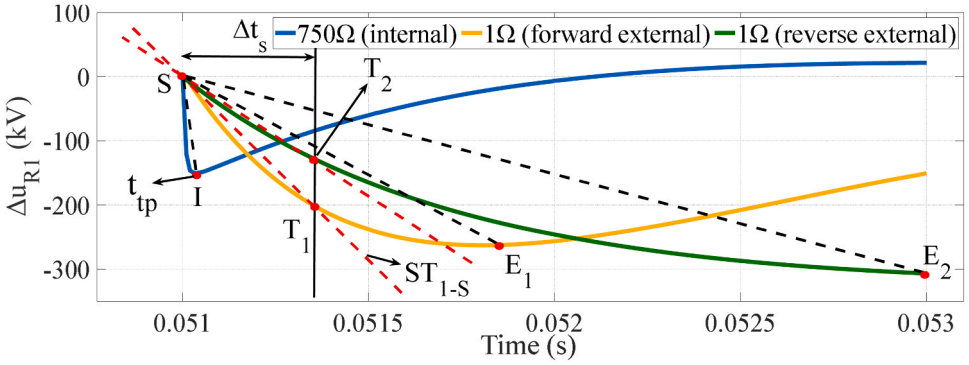

Fig. 10. Comparison of LFGVs of internal and external faults for design consideration under PTG and NTG faults.

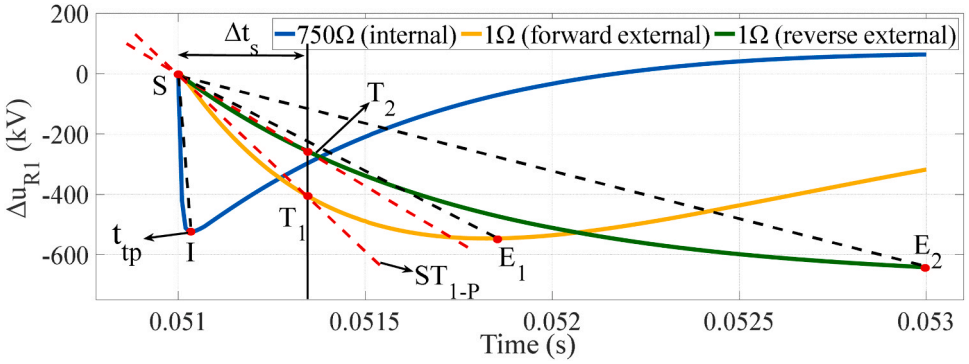

Fig. 11. Comparison of LFGVs of internal and external faults for design consideration under PTP faults.

$$C_p = \frac{1}{\sqrt{2}} \sum_{i=n_0-1}^{n_0+3} \left\{ u_{p,R1}(i) + u_{n,R1}(i) \right\} \tag{24}$$

$$\begin{cases} C_p < -V_{thp}, \ Positive\ pole \\ -V_{thp} < C_p < V_{thp}, \ Pole\ to\ pole \\ C_p > V_{thp}, \ Negative\ pole \end{cases} \tag{25}$$

where $u_{p,R1}$ and $u_{n,R1}$ are the positive and negative pole voltages at R_1, respectively. Based on the presented analytical calculations of Section 2, the threshold ($V_{th\text{-}p}$) is set 50 kV to ensure reliable identification of the fault pole under high-resistance internal and external faults.

The algorithm starts immediately when the SU in Eq. (23) is satisfied. After acquiring n_0 from the SU, Eq. (24) is checked to identify the faulty pole and adjust the threshold line accordingly. Afterward, based on the measured line-mode voltage at R_1, SDR_v is determined using Eq. (21). If SDR_v satisfies Eq. (22), a trip signal based on the results of FPIC is issued to the corresponding DC circuit breakers. Otherwise, the protective algorithm restarts.

4. Simulation results

The four-terminal MMC-HVDC grid, introduced in Section 2 is simulated in PSCAD/EMTDC as the test system. As illustrated in Fig. 1, fault scenarios are simulated to evaluate the performance of the proposed protection method under internal and external faults. All fault scenarios are initiated at $t = 50$ ms. Employing high sampling frequencies can lead to faster reaction times and more accurate calculation of SDR_v, despite the associated higher computational burden. nevertheless, extensive analytical calculations show that a good balance can be achieved by using a relatively low sampling frequency of 20 kHz.

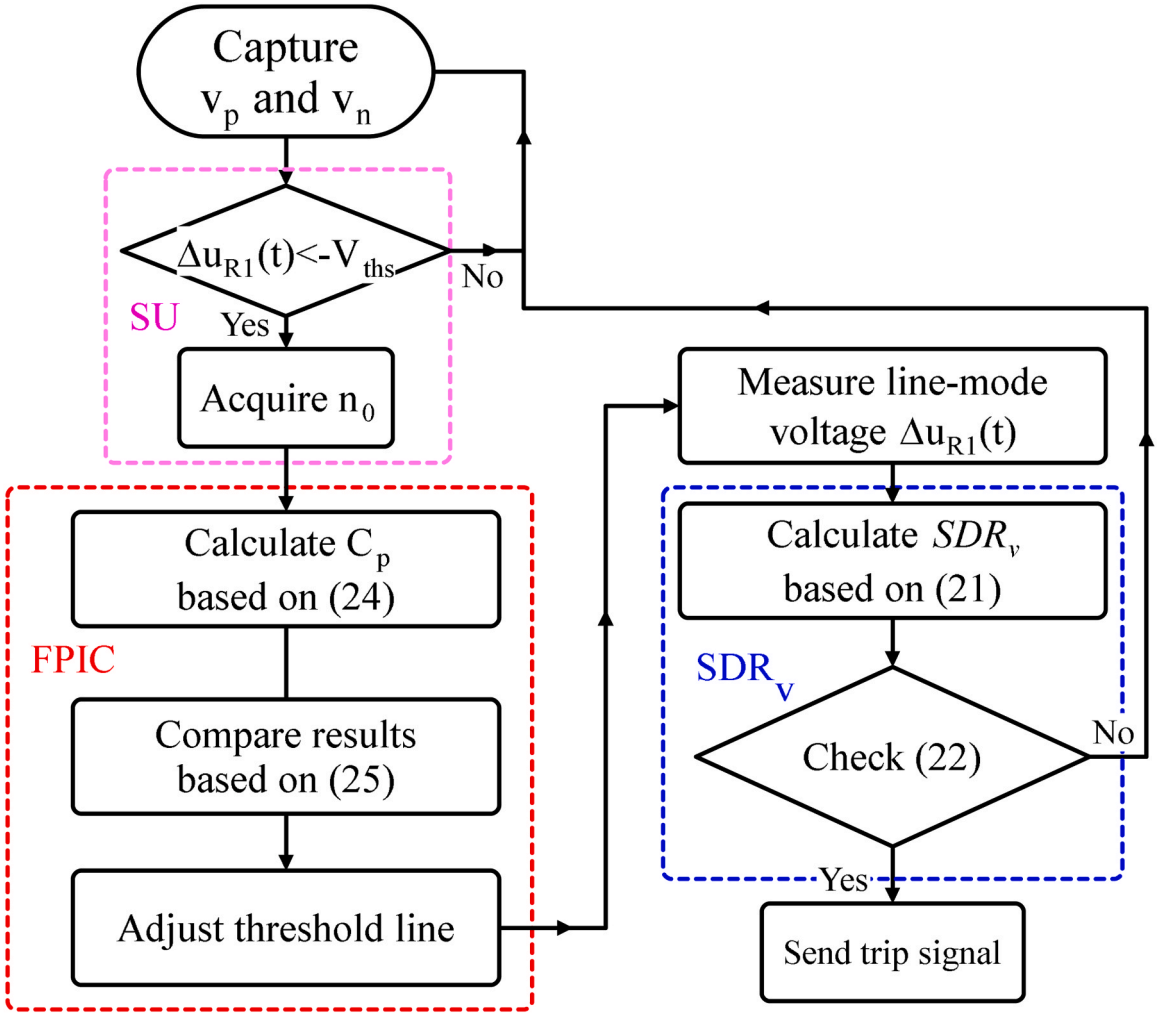

Fig. 12. Schematic diagram of the proposed protection algorithm.

Thus, according to Eq. (21), seven samples are used to calculate SDR_v, i.e., one and five samples before and after n_0, respectively; hence, Δt_1 and Δt_s are 350 and 250 μs, respectively. Since the performance of SU has been extensively discussed in previous works (Sneath et al., 2016; Leterme and Beerten, 2016), it will not be studied in this paper.

4.1. Internal faults

Fig. 13 (a) and (b) show the LFGV, $\Delta u_{R1}(t)$, under a 1-Ω PTG internal fault at 100 km and a 500-Ω PTG internal fault at 200 km, respectively. The results show that after the arrival of the fault signature at R_1, Δu_{R1} drops immediately. Consequently, SU is satisfied at 50.35 ms and then, SDR_v=-496.6 is calculated. Since SDR_v satisfies its threshold, $V_{th\text{-}s}$=-41, the internal fault is recognized at t = 50.4 ms. This has been shown in

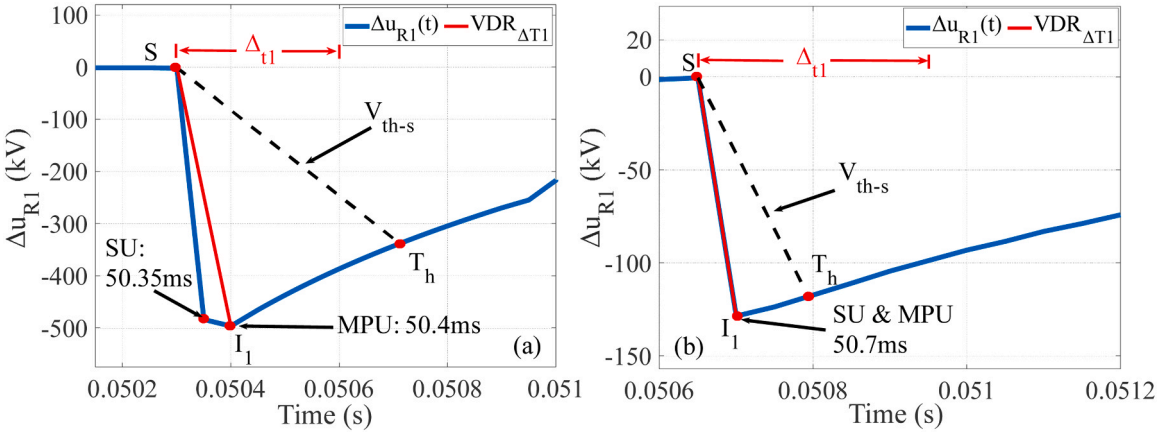

Fig. 13. $\Delta u_{R1}(t)$ and performance of the proposed protection method in identifying a) 1-Ω PTG internal fault at 100 km, b) 500-Ω PTG internal fault at 200 km.

Fig. 13 (a) where SDR_v and the threshold line are depicted by SI_1 and ST_h, respectively. It is clearly seen that SI_1 slope is sharper than ST_h, i.e., the proposed protection method reliably identifies this fault.

Similarly, Fig. 13 (b) shows the Δu_{R1} waveform for the 500-Ω PTG, which occurred at 200 km. In this condition, the SU is satisfied at $t =$ 50.7 ms and the minimum point is also discovered at the same time. In this case, SDR_v=-128.9 has a sharper slope compared to that of the threshold. Hence, this fault is precisely identified as well.

The analysis is carried out for PTP faults. In this context, a 1- and 500-Ω internal fault at 100 and 200 km are, respectively simulated and the results are presented in Fig. 14. For the 1- and 500-Ω faults, SDR_v is −1304.1 and −449.1, respectively. As displayed by ST_1 in Fig. 14 (a) and (b), the slope in both cases is sharper than their corresponding threshold lines, i.e., ST_h. Therefore, both internal faults are identified correctly.

In order to analyze the results in detail, Table 2 presents a summary of the results of various internal faults. Due to similar characteristics of NPG and PTG faults, the performance results of the PTG faults are solely presented in this Table. According to the results, FPIC, which calculates C_p, reliably identifies the fault pole in all cases. Consequently, the setting threshold is adjusted and SDR_v is measured. It can be seen that under all fault cases, SDR_v is lower than the corresponding threshold; hence, the proposed protection method is fully reliable in detecting internal faults at any location along the line with fault resistance of up to 1250 Ω.

The instant of issuing the trip signal is at the end of Δt_1, i.e., the time instant that the calculation process of SDR_v is finished. Therefore, due to the low computational burden of the proposed protective algorithm, the overall processing time, accounting for the data windows required for the process of SU, FPIC, and SDR_v is around Δt_1=0.35 ms. Accounting for the time delay of measurement sensors and subsequent data recording time (around 0.5–0.6 ms) (Xiang et al., 2019), the total action time of the proposed protection method is ∼0.9 ms. Therefore, in MMC-HVDC grids that require the protection principles to detect the DC faults within 3 ms, the proposed protection method meets the speed requirement.

As shown by the results of the near-end (10 km) and far-end (290 km and 300 km) fault scenarios, it is evident that the proposed protection method does not have a dead zone protection issue. In this way, it demonstrates its capability to detect faults at any location along the transmission line.

Table 2
Performance of the proposed protection method under various internal fault scenarios.

Fault type	Fault location (km)	Fault resistance (Ω)	C_p (kV)	SDR_v	Final decision
PTG	10	1	-2549	-544.4	Internal
		300	-1084	-149.4	Internal
		750	-593.7	-99.1	Internal
		1250	-395.4	-64.3	Internal
	50	1	-2551	-522.4	Internal
		300	-933	-189.2	Internal
		750	-476	-96.8	Internal
		1250	-310.4	-61.2	Internal
	100	1	-1784	-496.6	Internal
		300	-875	-182.7	Internal
		750	-448	-94.9	Internal
		1250	-288.2	-59.6	Internal
	150	1	-1788	-506.1	Internal
		300	-650	-185.4	Internal
		750	-441	-96.1	Internal
		1250	-286.8	-59.3	Internal
	200	1	-1201	-507.3	Internal
		300	-642	-183.5	Internal
		750	-433	-93.9	Internal
		1250	-255.5	-58.8	Internal
	250	1	-1204	-486	Internal
		300	-437	-176.6	Internal
		750	-324	-89.7	Internal
		1250	-211.4	-59.5	Internal
	290	1	-1086	-283	Internal
		300	-479.3	-188.6	Internal
		750	-399.2	-139.2	Internal
		1250	-266	-92	Internal
	300	1	-1190	-501.5	Internal
		300	-599.6	-257.3	Internal
		750	-344	-148.2	Internal
		1250	-235.3	-101.3	Internal
PTP	100	1	-2.3	-1304.1	Internal
		750	-2.2	-338.6	Internal
		1250	2.1	-112.7	Internal
	200	1	0.66	-1304.2	Internal
		750	-0.01	-338.4	Internal
		1250	-0.1	-113	Internal
	300	1	-0.5	-1281.5	Internal
		750	-1.1	-509.5	Internal
		1250	-2	-182.5	Internal

4.2. External faults

Another crucial aspect of the protection principles is their ability to perform reliably during external faults as presented in this subsection.

Fig. 15 shows Δu_{R1} (t) under a 50-Ω PTG forward external fault and reverse external fault at f_2 and f_3, respectively. In these cases, SDR_v is −23.4 and −15.5, respectively (shown by SE_1 in Fig. 15). It is evident from the results that the threshold is not exceeded in both cases. Therefore, these fault scenarios are correctly classified as external faults.

Moreover, Fig. 16 (a) and (b) illustrate Δu_{R1} (t) under an 1-Ω PTP external fault at f_4 and PTP external fault at f_5, respectively. Similar to the previous cases, since these external faults do not exceed their adjusted thresholds, they are correctly identified as external faults.

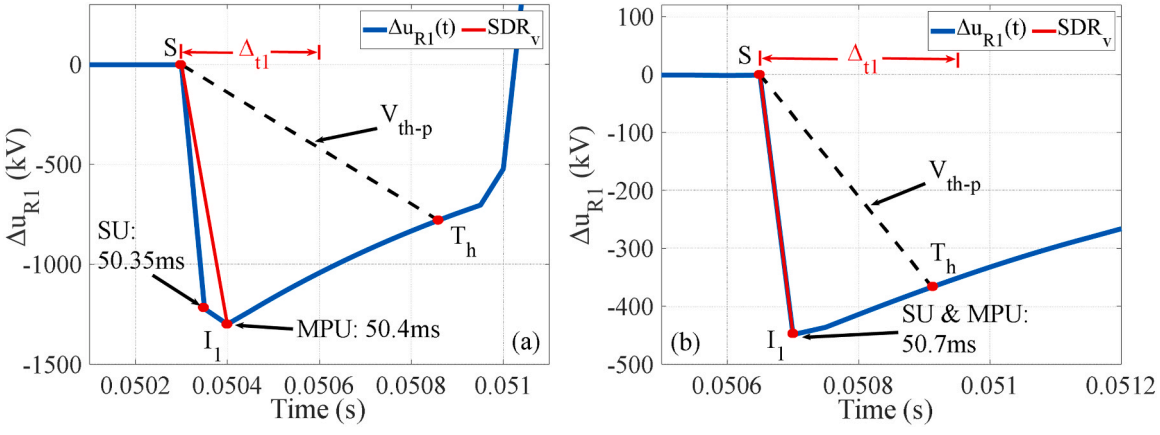

Fig. 14. Performance of the proposed protection method a) 1-Ω PTP internal fault at 100 km and b) 500-Ω PTP internal fault at 200 km.

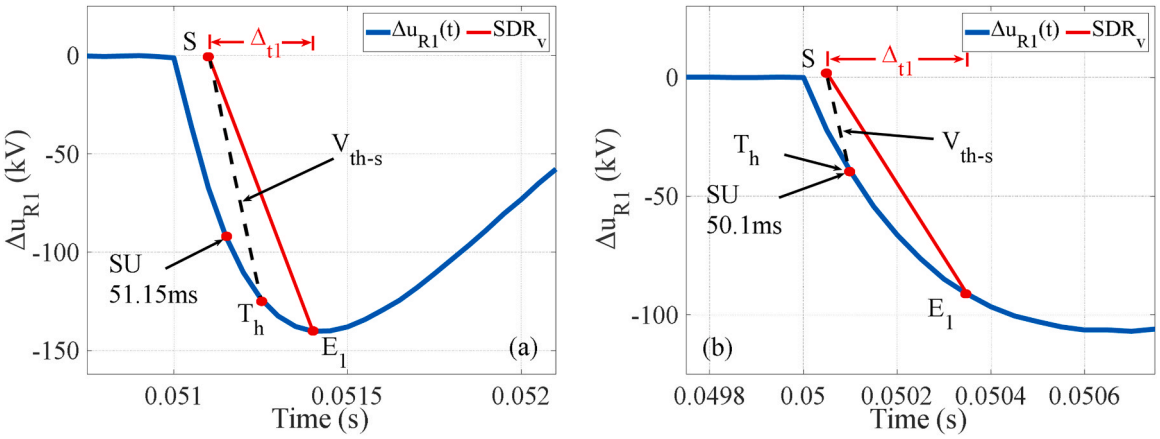

Fig. 15. Outputs for external fault simulation a) 50-Ω PTG forward external fault and b) 50-Ω PTG reverse external fault.

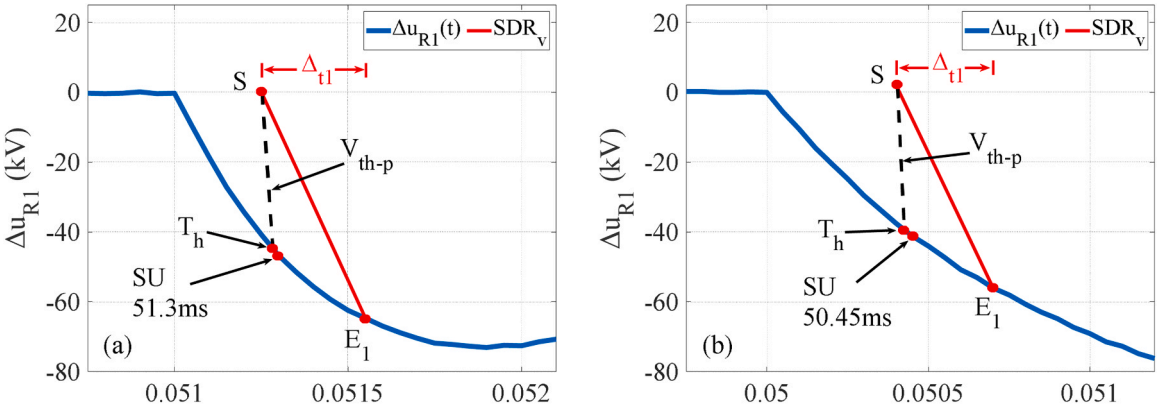

Fig. 16. $\Delta u_{R1}(t)$ and fault detection performance for a) 1-Ω PTP external fault at f_4 and b) 1-Ω PTP external fault at f_5.

A number of complementary results of the FPIC (C_p) and SDR_v under various external faults are also presented in Table 3. It is concluded from the results that the faulty pole is accurately identified in all cases. Furthermore, all fault scenarios are correctly recognized as external faults.

5. Robustness analysis and comparison with existing solutions

In this section, the effect of important variables, including CLI, measurement noise, converter clocking, and length of the transmission line on the performance of the proposed method is initially assessed. The overall performance of the proposed method is then highlighted through its comparison with existing classical schemes.

Table 3
Performance of the proposed protection method under various external fault scenarios.

Fault type	Fault location (km)	Fault resistance (Ω)	C_p (kV)	SDR_v	Final decision
PTG	f_2	50	-344.6	-23.4	External
	f_3		-530.7	-15.5	External
	f_2	300	-189.2	-24.2	External
	f_3		-241.1	-10.4	External
	f_4	1	-182	-4.8	External
	f_5		-199.7	-3.9	External
PTP	f_2	50	-0.18	-52.9	External
	f_3		-2.1	-36.8	External
	f_2	300	-1.6	-39.7	External
	f_3		1.9	-17.6	External
	f_4	1	0.05	-10.8	External
	f_5		2.9	-9.7	External

5.1. Sensitivity to the size of CLI

The impact of CLI on the results is investigated by re-tuning all CLIs to 25, 50, and 100 mH, and consequently, repeating the process of threshold determination as described in Figs. 10 and 11. The extracted threshold values accompanied with some performance results are presented in Table 4. According to the results, the faulty pole is correctly identified and the protection thresholds are adjusted accordingly. Finally, the comparison of the SDR_v results with the thresholds highlights promising performance for the proposed protection method in detecting internal faults under various CLI values, even as small as 25 mH.

5.2. Sensitivity to measurement noise

To investigate the performance of the proposed protection method under noise disturbance, a white Gaussian noise with 35 dB Signal-to-Noise ratio (SNR) is added to the measured voltage signals. The simulation results under a 750-Ω fault at 300 km and a PTG forward external fault at f_2 with 50 Ω are shown in Fig. 16 (a) and (b), respectively.

The results endorse that while the internal fault is reliably detected as its SDR_v passes the threshold, the proposed protection method remains inactive under the external fault.

The performance of the proposed protection method in detecting internal faults with different levels of noise disturbance is presented in Table 5, confirming the reliable performance of the proposed method. In

Table 4
Performance of proposed protection method under different CLI sizes.

Fault type	Fault location & resistance	CLI (mH)	C_p (kV)	SDR_v	$V_{th\text{-}s}$	$V_{th\text{-}p}$	Final decision
PTG	300 km 750Ω	25	-152.2	-106.6	-118.3	—	Mal-operation
		50	-218	-126.2	-69.3	—	Internal
		100	-287.7	-140.8	-54.9	—	Internal
PTP		25	-1.1	-363.3	—	-264.1	Internal
		50	-1	-432.6	—	-149.5	Internal
		100	-2.7	-481.6	—	-110.1	Internal

Table 5
Performance of Proposed Protection Method Under Noisy Measurements.

SNR	Cp (kV)	SDRv	Final decision
30	-352.5	-135.8	Internal
40	-347.2	-148.6	Internal
50	-351.4	-150.5	Internal

all cases, the fault occurs at 300 km with a fault resistance of 750 Ω.

5.3. Sensitivity to converter blocking

Converter blocking is an event that can cause severe voltage and current fluctuations on the DC side of the system, leading to a false operation of the protection methods. Therefore, various converter-blocking phenomena are simulated to examine the performance of the proposed method. In this context, Fig. 18 shows the performance of the proposed protection method under a converter blocking event at R_1. It is seen that SU is satisfied at 51.54 ms and SDR_v=-12.9 (SB_1 in Fig. 17). Hence, considering the protective threshold of −41, this phenomenon is not misclassified as a DC system fault. Hence, the reliability of the proposed method in converter-blocking scenarios is ensured.

5.4. Performance with longer transmission line and lower CLI

As shown in Figs. 10 and 11, the proposed protection method exhibits a great margin for fault detection. To explore the boundaries of the method, more extreme conditions are simulated by extending the transmission line length to 800 km and reducing the size of the CLI to 100 mH.

First, the new threshold values in accordance to the new conditions are obtained in a similar way conducted in Figs. 10 and 11. Fig. 19 (a) and (b) illustrate the analytical calculation of LFGV during an internal 1250-Ω fault at 800 km and a 1-Ω external fault at f_2, to be used for threshold determination. Based on the new results, the threshold values for PTG and PTP faults are determined to be $V_{th\text{-}s} = -51$ and $V_{th\text{-}p} = -108.5$, respectively.

Further simulations are carried out in the most challenging fault cases to evaluate the performance of the proposed protection method under these new scenarios. As summarized in Table 6, the SDR_v values for internal PTG and PTP 1250-Ω faults at line ends are −86.5 and −137.5, which exceed their corresponding thresholds. As a result, these faults are accurately identified.

Overall, it is evident that the proposed protection method is reliable in detecting internal faults along a 800-km transmission line up to a fault resistance of 1250 Ω.

5.5. Comparison with existing solutions

The main contribution of this study is to demonstrate improvements over transient-based protection methods, particularly ROCOV-based solutions. However, being a TW-based approach, the proposed protection method offers distinct advantages compared to other TW-based solutions, which are also demonstrated here. As summarized in Table 7, the following conclusions can be derived.

5.5.1. Comparison to transient-based methods

The most commonly used ROCOV-based methods are those presented in Sneath et al. (2016) and Leterme and Beerten (2016). In comparison, the proposed method offers improved selectivity and sensitivity in fault detection and requires less sampling frequency. Additionally, determining thresholds in Sneath et al. (2016) and Leterme and Beerten (2016) is challenging due to the lack of analytical calculations, whereas the proposed method benefits from robust analytical calculations, making it a more straightforward and applicable solution.

When it comes to transient voltage derivative-based methods such as Li et al. (2017), Li et al. (2018), and Liu et al. (2017), these approaches heavily rely on CLI magnitude and suffer from reduced selectivity when lower CLIs are used. Additionally, noise can adversely affect the performance in Li et al. (2017) and Li et al. (2018). However, the proposed protection method addresses these drawbacks by carefully calculating SDR_v using LFVG over a data window of Δt_1, which significantly reduces the impact of noise and CLI. Moreover, the overall sensitivity of these methods (100–400Ω) is lower than that of the proposed protection method (up to 1250Ω).

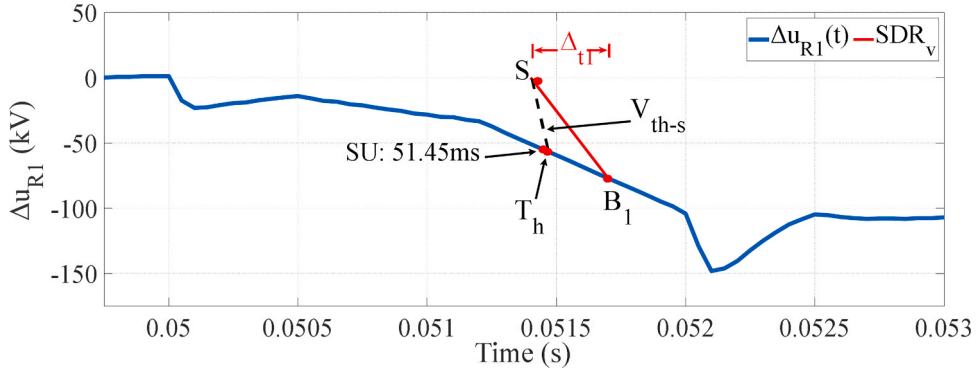

Fig. 18. Effect of converter blocking at R_1 on the performance of the proposed method.

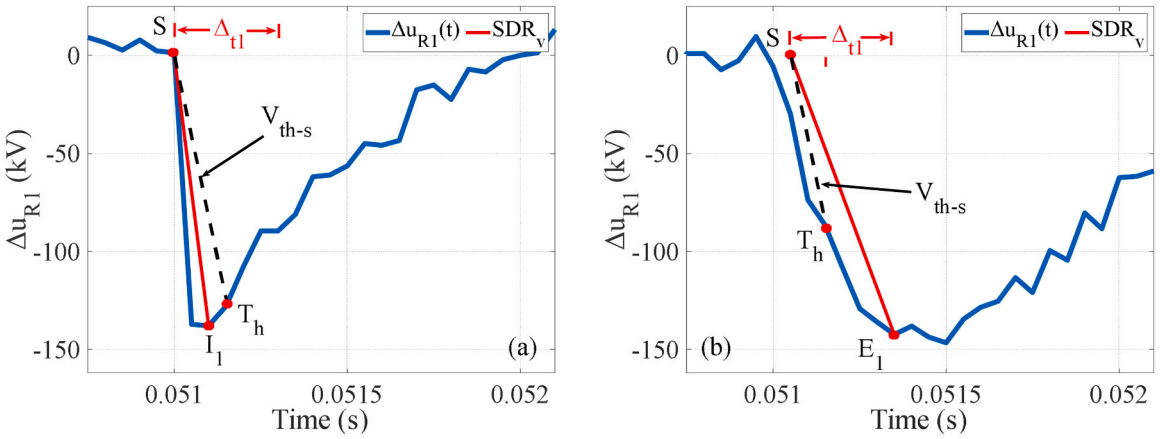

Fig. 17. $\Delta u_{R1}(t)$ and performance of the proposed protection method in detecting a) 750-Ω PTG internal fault at 300 km and b) 50-Ω PTG forward external fault.

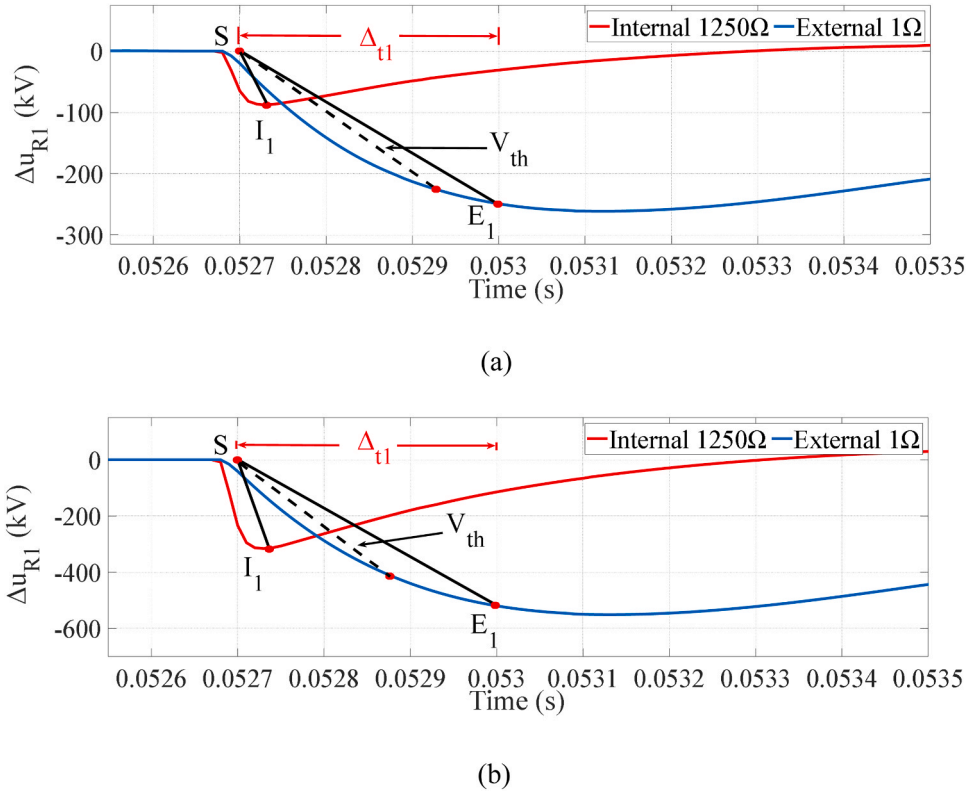

Fig. 19. Analytical calculation of LFGV under new conditions and the process of threshold calculations a) PTG fault b) PTP fault.

Table 6
Performance of proposed protection method under 1250-Ω PTG and PTP internal faults.

Fault type	Fault location	resistance	SDR_v	Final decision
PTG	800 km	1250Ω	-86.5	Internal
PTP			-137.5	

5.5.2. Comparison to TW-based methods

The proposed protection method distinguishes internal faults at any location along the transmission line with resistance up to 1250 Ω. In contrast, the previous methods presented in Table 7 detect faults with resistances ranging from 200–600 Ω. Therefore, the proposed method provides the advantage of fault identification for larger fault resistances.

Action time is still a challenge for pilot protection schemes. As an example, for fiber optic cables with a 200 km/ms communication delay (Lan et al., 2021), the time to transfer data from one side of the 300 km transmission line of the test grid to the other side of the line would be at least 1.5 ms. This time delay would be even more prominent for lengthier transmission lines. On top of that, other time-consuming matters, such as data synchronization add to the action time of such methods. Conversely, the proposed method is a single-end solution and does not require double-end measurements, data synchronization, and data exchange via a communication link. Therefore, the speed of protection, which is a crucial matter in MMC-HVDC protection, is higher in the proposed protection method compared to those proposed in Li et al. (2020a) and Yu et al. (2021), i.e., the action time is ~3 ms in Li et al. (2020a) and Yu et al. (2021), which is noticeably higher than the action time of the proposed method (less than 1 ms). The action time of the proposed protection method is also shorter than those in Lan et al.

Table 7
Comparison to similar traveling-wave methods.

Reference number	Detectable high-resistance fault	Protection action time	Sampling frequency	Accuracy in analytical calculation
Transient-based methods				
(Sneath et al., 2016), (Leterme and Beerten, 2016)	100–200Ω	~200μs	~100 kHz	low
(Li et al., 2017)	200–400Ω	<1.5 ms	~100 kHz	low
(Li et al., 2018), (Liu et al., 2017)	~350Ω	<2 ms	—	low
TW-based methods				
(Zhang et al., 2021)	~500Ω	<1 ms	200 kHz	medium
(Li et al., 2020a)	~300Ω	~3 ms	10 kHz	low
(Yu et al., 2021)	>400Ω	>3 ms	10 kHz	medium
(Lan et al., 2021)	>300Ω	>3 ms	>10 kHz	low
(Zhang et al., 2019)	~500Ω	<1.3 ms	25 kHz	low
(Li et al., 2019)	~300Ω	~2 ms	10 kHz	medium
(Xiang et al., 2019)	~200Ω	>2 ms	20 kHz	medium
(Yu et al., 2023a)	<600Ω	variable	100 kHz	high
(Lan et al., 2022)	~600Ω	>1 ms	≥50 kHz	low
(Yu et al., 2023b)	<500Ω	-	100 kHz	low
Proposed method	~1250Ω	<1 ms	20 kHz	high

(2021) and Li et al. (2019), mainly due to shorter data window and lower computational burden. The approach used in Yu et al. (2023a) relies on reflected traveling waves from the fault point and remote-end DC terminal for fault identification, which introduces a dependency on fault location, while the method in (Yu et al., 2023b) uses multiple data fitting processes, leading to an increased computational burden. Therefore, both methods are noticeably slower than the proposed protection method.

Presented methods in Zhang et al. (2021) and Zhang et al. (2022) lack a robust analytical calculation of LFGV, requiring numerous simulation scenarios to determine threshold values in their algorithms. Conversely, this study exploits the analytical presentation of LFGV with extended accuracy under various fault locations and resistances, as demonstrated earlier. This ensures a robust threshold calculation as well as a reliable protective operation under both internal and external fault scenarios. Moreover, (Zhang et al., 2021) relies solely on the wavefront time of the initial fault-generated TW to distinguish internal faults. Consequently, it has lower sensitivity and selectivity compared to the proposed protection criterion, SDR_v, which uses both the wavefront time and DM of the LFGV for fault identification.

6. Conclusion

In this paper, a new primary protection method based on the selective drop rate of LFGV is proposed. The proposed protective criterion is established upon analytical calculation of LFGV under various internal and external faults. The protective criterion is defined as the slopes of the straight lines connecting the starting points of the LFGVs to their wave heads. Through analytical calculations, it is discussed that the protective criterion produces significantly sharper slopes under internal faults compared to those under external faults, which reliably distinguishes internal and external faults.

Compared to ROCOV and similar transient-based solutions, the proposed protection method exhibits faster response and higher sensitivity and selectivity in detecting internal faults up to 1250 Ω at any location along the line. Additionally, it demonstrates higher reliability under non-fault phenomena such as converter-blocking incidents and noise disturbances. The robustness analysis shows that the proposed protection method performs reliably under different transmission line lengths and CLI sizes. More importantly, the analytical calculations provide improved accuracy in comparison to similar studies and a solid foundation for extracting the protective threshold values, which are other advantages of the proposed protection method even in comparison to more advanced TW-based solutions.

The preliminary evaluations of the proposed protection method have shown reliable performance in case of lightning disturbance. However, considering the complexity and critical importance of studying lightning disturbances, it is deemed more suitable to cover this topic in future works, and also add hardware-in-loop tests to further validate the practicality of the proposed protection method.

Author Statement

The authors, hereby, declare that:

- This paper has not been published previously and it is not under consideration for publication elsewhere
- Its publication is approved by all authors and tacitly or explicitly by the responsible authorities where the work was carried out
- If accepted, it will not be published elsewhere in the same form, in English or in any other language, including electronically without the written consent of the copyright-holder.

CRediT authorship contribution statement

Farzad Dehghan Marvasti: Writing – review & editing, Writing – original draft, Methodology, Investigation, Conceptualization. **Ahmad Mirzaei:** Supervision, Investigation. **Mehdi Savaghebi:** Supervision. **Aleksandra Lekić:** Supervision. **Marjan Popov:** Supervision.

Declaration of Competing Interest

The authors declare that they have no known competing financial interests or personal relationships that could have appeared to influence the work reported in this paper.

Data Availability

No data was used for the research described in the article.

References

Chandio, R.H., Chachar, F.A., Soomro, J.B., Ansari, J.A., Munir, H.M., Zawbaa, H.M., Kamel, S., 2023. Control and protection of MMC-based HVDC systems: a review. Energy Rep. 9, 1571–1588.
Chen, L., Zhao, Z., Qiao, X., Li, G., Chen, H., 2022. A novel current-limiting method for MMC-HVDC by coordinating virtual impedance control and fault current limiter. Energy Rep. vol. 8, 385–398.
Chu, X., 2019. Transient numerical calculation and differential protection algorithm for HVDC transmission lines based on a frequency-dependent parameter model. Int. J. Electr. Power Energy Syst. 108, 107–116.
Dai, Z., Liu, N., Zhang, C., Pan, X., Wang, J., 2020. A pilot protection for HVDC transmission lines based on transient energy ratio of DC filter link. IEEE Trans. Power Del. 35 (4), 1695–1706.
Farshad, M., 2021. A pilot protection scheme for transmission lines of half-bridge MMC-HVDC grids using Cosine distance criterion. IEEE Trans. Power Del. 36 (2), 1089–1096.
Jovcic, D., Lin, W., Nguefeu, S., Saad, H., 2018. Low-energy protection system for DC grids based on full-bridge MMC converters. IEEE Trans. Power Del. 33 (4).
Lan, T., Li, Y., Duan, X., 2021. High fault-resistance tolerable traveling wave protection for multi-terminal VSC-HVDC. IEEE Trans. Power Del. 36 (2), 943–956.
Lan, T., Xiao, H., Li, Y., Chen, J., 2022. Computationally effective frequency transient-based transmission line protection for multiterminal VSC-HVdc. IEEE Trans. Industr Inform 18 (9), 5925–5935.

Leterme, W., Beerten, J., Van Hertem, D., 2016. Nonunit protection of HVDC grids with inductive DC cable termination. IEEE Trans. Power Del. 31 (2), 820–828.
Li, A., Cai, Z., Sun, Q., Li, X., Ren, D., Yang, Z., 2009. Study on the dynamic performance characteristics of HVDC control and protections for the HVDC line fault. Calgary, Canada, pp. 1–5.
Li, B., Li, Y., He, J., Wen, W., 2019. A novel single-ended transient-voltage-based protection strategy for flexible DC grid. IEEE Trans. Power Del. 34 (5), 1925–1937.
Li, B., Lv, M., Li, B., Xue, S., Wen, W., 2020b. Research on an improved protection principle based on differential voltage traveling wave for VSC-HVDC transmission lines. IEEE Trans. Power Del. 35 (5), 2319–2328.
Li, B., Li, Y., He, J., Li, B., Liu, S., Liu, b, Xu, L., 2020a. An improved transient traveling-wave based direction criterion for multi-terminal HVDC grid. IEEE Trans. Power Del. 35 (5), 2517–2529.
Li, C., Gole, A., Zha, C., 2018. A fast DC fault detection method using DC reactor voltages in HVdc grids. IEEE Trans. Power Del. 33 (5), 2254–2264.
Li, R., Xu, L., Yao, L., 2017. DC fault detection and location in meshed multi-terminal HVDC systems based on DC reactor voltage change rate. IEEE Trans. Power Del. 32, 1516–1526.
Liu, J., Tai, N., Fan, C., 2017. Transient-voltage-based protection scheme for DC line faults in the multiterminal VSC-HVDC system. IEEE Trans. Power Del. 32 (3), 1483–1494.
Liu, L., Lekić, A., Popov, M., 2023. Robust traveling wave-based protection scheme for multiterminal DC grids. IEEE Trans. Power Del. 1–13. https://doi.org/10.1109/TPWRD.2023.3265748.
Marvasti, F.D., Mirzaei, A., Golshan, M.E.H., 2020. Novel pilot protection scheme for line-commutated converter high voltage direct current transmission lines based on behaviour of characteristic harmonic impedances. IET Gener. Transm. Distrib. 15 (2), 264–278.
Saizhao, Y., Wang, X., Jinyu, W., 2021. An improved DC fault protection scheme independent of boundary components for MMC based HVDC grids. IEEE Trans. Power Del. 36 (4), 2520–2531.
Saleh, K.A., Hooshyar, A., El-Saadany, E.F., Zeineldin, H.H., 2020. Protection of high-voltage DC grids using traveling-wave frequency characteristics. IEEE Syst. J. 14 (3), 4284–4295.
Sneath, J., Rajapakse, A.D., 2016. Fault detection and interruption in an earthed HVDC grid using ROCOV and hybrid DC breakers. IEEE Trans. Power Del. 31 (3), 973–981.
Sun, P., Li, Y., Qu, L., Gong, J., Li, H., Huang, S., 2023. Negative sequence current accumulation difference based wind farm collection line protection for MMC-HVDC system. Energy Rep. 9, 249–258.
Wang, H., Qi, Z., Fu, L., Liu, F., Hu, J., Dong, X., Li, W., 2021. Fast and reliable differential protection based on traveling waves for HVDC transmission line. Energy Rep. 7, 619–628.
Wang, Y., Hao, Z., Zhang, B., Kong, F., 2019. A pilot protection scheme for transmission lines in VSC-HVDC grid based on similarity measure of traveling waves. IEEE Access 7, 7147–7158.
Xiang, W., Yang, S., Xu, L., Zhang, J., Lin, W., Wen, J., 2019. A transient voltage-based DC fault line protection scheme for MMC-based DC grid embedding DC breakers. IEEE Trans. Power Del. 34 (1), 334–345.
Yu, D.C., Zhou, N.C., Liao, J.Q., Wang, Q.G., Wei, N.Q., 2023b. Non-unit ultra-high-speed DC line protection method for HVDC grids using dynamic fitting algorithm with data reconstruction. Int. J. Electr. Power Energy Syst. 154, 109469.
Yu, X., Xiao, L., 2021. A DC fault protection scheme for MMC-HVDC grids using new directional criterion. IEEE Trans. Power Del. 36 (1), 441–451.
Yu, X., Gu, J., Zhang, X., Mao, J., Xiao, L., 2023a. A self-adaptation non-unit protection scheme for MMC-HVDC grids based on the estimated fault resistance. Int. J. Electr Power Energy Syst. 152, 109263.
Zaang, Y., Li, Y., Song, J., Li, B., Chen, X., 2019. A new protection scheme for HVDC transmission lines based on the specific frequency current of DC filter. IEEE Trans. Power Del. 34 (2), 420–429.
Zhang, C., Song, G., Dong, X., 2021. Non-unit ultra-high-speed DC line protection method for HVDC grids using first peak time of voltage. IEEE Tran. Power Del. 36 (3), 1683–1693.
Zhang, C., Li, Y., Song, G., Dong, X., 2022. Fast and sensitive nonunit protection method for HVDC grids using Levenberg–Marquardt algorithm. IEEE Trans. Ind. Electron. 69 (9), 9064–9074.
Zhang, F., Han, K., Yu, X., Wu, J., Chen, Y., Wen, M., 2023. A novel pilot differential protection for HVDC transmission line based on the differential voltage. Energy Rep. 9, 680–686.
Zhang, S., Zou, G., Wang, C., Li, J., Xu, B., 2019. A non-unit boundary protection of DC line for MMC-MTDC grids. Int. J. Electr. Power Energy Syst. 116 (6).
Zhang, Y., Tai, N., Xu, B., 2012. Fault analysis and traveling-wave protection scheme for bipolar HVDC lines. IEEE Trans. Power Del. 27 (3), 1583–1591.